Journal of Biomedical Optics

BiomedicalOptics.SPIEDigitalLibrary.org

Mechanically switchable solid inhomogeneous phantom for performance tests in diffuse imaging and spectroscopy

Antonio Pifferi
Alessandro Torricelli
Rinaldo Cubeddu
Giovanna Quarto
Rebecca Re
Sanathana K. V. Sekar
Lorenzo Spinelli
Andrea Farina
Fabrizio Martelli
Heidrun Wabnitz

SPIE.

Mechanically switchable solid inhomogeneous phantom for performance tests in diffuse imaging and spectroscopy

Antonio Pifferi,[a] Alessandro Torricelli,[a] Rinaldo Cubeddu,[a,b] Giovanna Quarto,[a] Rebecca Re,[a] Sanathana K. V. Sekar,[a] Lorenzo Spinelli,[b] Andrea Farina,[b] Fabrizio Martelli,[c,*] and Heidrun Wabnitz[d]
[a]Politecnico di Milano, Dipartimento di Fisica, Piazza Leonardo da Vinci 32, Milano 20133, Italy
[b]Istituto di Fotonica e Nanotecnologie, Consiglio Nazionale delle Ricerche, Piazza Leonardo da Vinci 32, Milano 20133, Italy
[c]Università degli Studi di Firenze, Dipartimento di Fisica e Astronomia, Via G. Sansone 1, Firenze, Sesto Fiorentino 50019, Italy
[d]Physikalisch-Technische Bundesanstalt (PTB), Abbestraße 2-12, Berlin 10587, Germany

Abstract. A mechanically switchable solid inhomogeneous phantom simulating localized absorption changes was developed and characterized. The homogeneous host phantom was made of epoxy resin with black toner and titanium dioxide particles added as absorbing and scattering components, respectively. A cylindrical rod, movable along a hole in the block and made of the same material, has a black polyvinyl chloride cylinder embedded in its center. By varying the volume and position of the black inclusion, absorption perturbations can be generated over a large range of magnitudes. The phantom has been characterized by various time-domain diffuse optics instruments in terms of absorption and scattering spectra, transmittance images, and reflectance contrast. Addressing a major application of the phantom for performance characterization for functional near-infrared spectroscopy of the brain, the contrast was measured in reflectance mode while black cylinders of volumes from ≈20 mm^3 to ≈270 mm^3 were moved in lateral and depth directions, respectively. The new type of solid inhomogeneous phantom is expected to become a useful tool for routine quality check of clinical instruments or implementation of industrial standards provided an experimental characterization of the phantom is performed in advance. [DOI: 10.1117/1.JBO.20.12.121304]

Keywords: tissue-like phantoms; diffuse optical imaging; performance characterization; diffuse optics.

Paper 150083SSR received Feb. 11, 2015; accepted for publication Jun. 5, 2015; published online Jul. 28, 2015.

1 Introduction

Diffuse optics[1] provides noninvasive tools to investigate highly scattering media (e.g., biological tissues in the wavelength range from 600 to 1300 nm) of large volumes (cubic centimeters) and depths up to a few centimeters beneath the surface. Both chemical (related to absorption) and structural (related to scattering) information can be retrieved by photons traveling through the diffusive medium. Numerous applications have been pursued, both in the medical field—ranging from functional brain imaging[2,3] and neuromonitoring,[4–6] to cancer diagnostics[7,8] and therapy monitoring,[9,10]—and in industrial sectors such as characterization of food,[11,12] wood,[13,14] and pharmaceuticals.[15,16] A key requirement for such applications to grow and gain a more widespread clinical or industrial acceptance is to achieve a high grade of reliability, reproducibility, accuracy in quantification, and comparability of clinical results.[17] There is a compelling need to nurture the culture of quality assessment and quantitative grading of instruments in diffuse optics to support the parallel development of new instruments/techniques and applications on a stringent basis.[18–20]

The main path to reach these goals is the adoption of protocols for performance assessment to measure and characterize the system behavior. Recalling only the initiatives that gathered consensus among many laboratories, we can quote the "BIP protocol"[18] for the assessment of basic instrument performances of time-domain diffuse optics instruments, in terms of key parameters related to fundamental features of the system, such as responsivity (overall light detection capability), time resolution (temporal instrument response function), and stability. A different aim was pursued in the "MEDPHOT protocol,"[20] which considers the system as a "black box" to be assessed in terms of its capability in measuring the optical properties of a homogeneous medium. The protocol allows the evaluation of different characteristics such as the accuracy, linearity, stability, reproducibility, and noise level in the retrieval of the absorption and scattering coefficients. The "nEUROPt protocol"[19] followed a similar approach, but dealt with the determination of localized absorption changes, as in the case of brain imaging. In particular, the instruments are characterized with respect to sensitivity (contrast and contrast-to-noise ratio), spatial resolution (lateral resolution and depth selectivity), and quantitation (accuracy and linearity). In the context of the multicenter clinical trial of the American College of Radiology Imaging Network (ACRIN) to measure the breast tumors response to neoadjuvant chemotherapy by means of diffuse optical spectroscopic imaging, phantom tests were performed for quality control, to assess operator and instrument reliability.[21] At last, we note that also in the field of tissues fluorescence imaging, phantoms were developed to characterize and compare imaging systems and to train surgeons.[22]

*Address all correspondence to: Fabrizio Martelli, E-mail: fabrizio.martelli@unifi.it

Each protocol for performance assessment is implemented by means of a specific class of phantoms, suitable to mimic the situation being relevant in the clinical application in a controlled and reproducible way. For instance, the BIP protocol implemented the responsivity measurement by means of a solid slab phantom with spectrally characterized diffuse transmittance to mimic the amount and angular distribution of light exiting biological tissues. The "MEDPHOT protocol" required a matrix of homogeneous phantoms combining a set of 32 different absorption coefficients and different scattering coefficients (32 values = 8 absorption values × 4 scattering values). A practical kit based on solid phantoms was produced about 10 years ago and since then has been circulated to many laboratories all over the world. In the ACRIN project, two sets of identical homogeneous phantoms (silicone-rubber and polyurethane based, with different absorption and scattering spectra) were distributed to all partners. The nEUROPt protocol was initially implemented by means of a tank filled with intralipid and ink dilutions and using a set of black polyvinyl chloride (PVC) cylinders to simulate absorption perturbations.[19,23] The high accuracy in the characterization of the liquid phantom properties[24] was an essential prerequisite for an excellent agreement between experimental measurements and theoretical predictions.[23]

We propose here a new kind of inhomogeneous phantoms suitable to implement parts of the nEUROPt protocol with more ease than by liquid phantoms, particularly for quality control in a clinical setting. More generally, this phantom can be used to simulate any clinical problems related to a localized change in absorption properties, such as functional brain imaging, detection and characterization of breast tumors, and monitoring of tumor reduction after neoadjuvant chemotherapy. The following key requirements shall be met: (1) robustness and ease of use for quick routine applications in a clinical setting; (2) durability and reproducibility to provide consistent reference during clinical studies; (3) applicability to different instruments and clinical problems to offer a general purpose tool for widespread use; (4) manufacturability to permit potential implementation in industrial standards; and (5) suitability to simulate localized changes in the absorption coefficient.

Different solutions for the construction of inhomogeneous phantoms were proposed, as shown in the review papers[25,26] and in a recent special issue of Biomedical Optics Express,[17] adopting liquid–liquid,[27] liquid–solid,[28–30] and solid–solid structures,[31–34] each of them with different advantages and criticalities. To comply with the requirements (1), (2), and (4) we opted for a solid–solid approach, obviously more practical than liquid–liquid or mixed approaches. We fulfilled requirements (3) and (5) by inserting a movable black inclusion within the phantom that can be translated far from (homogeneous case) or beneath (inhomogeneous case) the measurement site.

The use of black inclusions was motivated by the following considerations: a totally absorbing inclusion can mimic a realistic absorption perturbation for a wide range of optical properties, geometries, and operating conditions.[35] This assumption is based on an equivalence relation that links inclusions producing the same effect in terms of absorption perturbation. One completely absorbing spherical inclusion with a given volume is equivalent to absorption inhomogeneities with different combinations of the absorption change $\Delta\mu_a$, volume, and shape, all producing the same contrast in the measurement. This equivalence was shown to be valid both for time-resolved (TR) and continuous-wave (CW) approaches and to be fairly independent of the measurement geometry, source–detector separation, and location of the inhomogeneity as well as of the background absorption coefficient (μ_a). Apart from a few extreme cases—as for very low-absorption perturbations quite close to a source or a detector or to the external boundary of the medium—the relation is valid in general. The key advantage of the use of totally absorbing inclusions is that the large variety of possible combinations of absorption properties, volumes, and shapes related to different clinical problems are all described in first order by a set of e.g., 4 or 5 black inclusions of different volumes. The production and characterization of these inclusions are straightforward, being related only to their volume. Their effect can be easily converted into finite absorption changes within a given larger volume by means of empirical equations.[23] The equivalent black volume could be even adopted as a universal parameter to grade the strength of a perturbation.[35]

Inhomogeneous phantoms can be classified by the different techniques used to obtain the absorption inclusion inside the background medium. Among the techniques used to build dynamic phantoms can be mentioned thermochromic, electrochromic, and mechanical phantoms. In thermochromic phantoms, variable localized absorption changes were produced by localized heating of targets impregnated with a thermochromic pigment.[32] In electrochromic liquid-crystal-based phantoms, the active element is an electrochromic cell whose optical properties can be adjusted electronically.[36,37] Both thermochromic and electrochromic phantoms allow gradual dynamic (time-varying) absorption changes to be mimicked, but a quantitative grading of the magnitude of the absorption change is not feasible. In both cases, the position of the absorbing inclusion is fixed. In mechanical solid phantom, a solid inclusion is mechanically inserted and moved inside a solid background medium. A two-layered phantom with mechanical movement was employed to mimic hemoglobin changes in superficial and deep tissues.[34] Mechanical solid phantoms have a better control and reproducibility of the absorption changes compared to the other types of phantoms, while they offer lesser capabilities to reproduce dynamic changes. The switchable phantom here implemented can be classified as a mechanical solid phantom.

In the following, we present a first practical implementation of such phantom concept, still open for further refinements. We first describe the phantom construction (Sec. 2), then we introduce the time-domain experimental setups used to characterize the phantom (Sec. 3), and then finally we demonstrate its properties using a spectroscopy system for spectral characterization, an imaging system to study spatial heterogeneities, and a system for TR functional near-infrared spectroscopy to record the homogeneous-to-inhomogeneous contrast (Sec. 4).

2 Phantom Design and Construction

The switchable phantom was designed as composed of two parts: a homogeneous host phantom and a movable rod. The host phantom has a cylindrical hole in which the rod can be inserted (see Fig. 1). By moving the rod which carries a black cylindrical inclusion, the phantom can be switched from a homogeneous to an inhomogeneous phantom. The host phantom is manufactured from a solid homogeneous base material consisting of epoxy resin (NM500/H179B; Nils Malmgren AB, Ytterby, Sweden) to which black toner (black 46/I, part No. 885 983 06, Infotec, France) and TiO_2 particles (T-8141, Sigma–Aldrich, St. Louis, Missouri) were added as absorption and

scattering components, respectively. The phantom recipe was taken from the work of Swartling et al.,[38] but we introduced some improvements to better control the reproducibility and the quality of the final product. One hundred twenty mg of black toner powder was dispersed in 100-g hardener by sonicating for 20 min (B220, Branson Ultrasonics, Danbury) to prepare the absorption base from which the required amount was taken and added to the final volume of hardener. The TiO_2 powder was directly weighted to the proper amount. The resin was poured in the mold (Jars Nalgene style 2118, 500 ml, Sigma–Aldrich, St. Louis, Missouri), the TiO_2 particles were added and then mechanically dispersed in the resin by means of a laboratory homogenizer (OV5, VELP Scientifica, Italy) operating for 3 to 5 min at 10,000 rpm. To this suspension, the mixture of hardener and black toner were added, and then a mechanical stirring was performed for 2 to 3 min at 12,000 rpm. A vacuum pump (XDS5, Edwards Ltd, Crawley, UK), operating at 10 to 20 mbar was used to eliminate air bubbles (usually 4 to 5 min pumping). Since the mechanical stirring overheats the mixture, following the bubble removal, the mold was kept partially immersed in running water for about 10 min to bring the mixture to room temperature. Then, the phantom was cured in a ventilated oven (UTP 20, Heraeus, Heraeus Holding GmbH, Hanau, Germany) at 50°C for 6 to 8 h. The phantom was then extracted from the mold, ready to be machined in the proper shape, and polished. A cylindrical hole (diameter 14 mm) was finally drilled parallel to the largest surface at a depth of 15 mm (Fig. 1). The concentration of black toner and TiO_2 for the host phantom were chosen so as to yield an absorption coefficient, μ_a, of 0.1 cm^{-1} and a reduced scattering coefficient, μ_s', of 10 cm^{-1} at 690 nm, representative of average biological tissue optical properties in the 600 to 1000 nm spectral range.

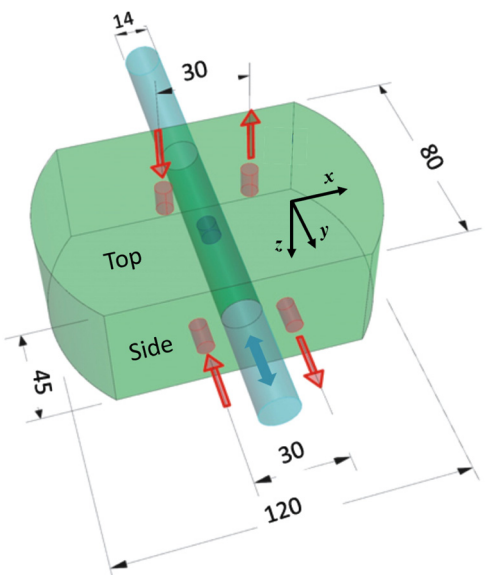

Fig. 1 Schematic of the phantom. The rod with an embedded black polyvinyl chloride (PVC) cylinder can be translated within the phantom block. The center of the cylinder is located at the center of the rod. The optical fiber probes are represented by small cylinders with the arrows indicating the source and detector. The probes are fixed either on the top surface for a lateral scan or on the side surface for a depth scan of the absorber. The corresponding axes are indicated in the figure. All the dimensions shown are in millimeters. For further details see text.

To build the moving part of the phantom, four small plexiglass containers ($20 \times 20 \times 200$ mm^3 inner sizes) were prepared. To mimic realistic changes in absorption properties, small black PVC cylinders with different diameters and lengths as listed in Table 1 were made for inclusions. Each PVC cylinder was positioned at the center of the container by being glued onto a small pedestal of solid epoxy resin which was installed in the container. It had the same optical properties as those of the base material of the phantom (i.e., not introducing in principle any perturbation in the optical properties).

Then, liquid epoxy resin remaining from the preparation of the base material, i.e., with the same optical properties, was poured into the containers and cured. The four square rods were then carefully machined to manufacture four cylindrical rods (with a diameter of 14 mm and a length of 180 mm) with a diameter tolerance suitable to allow smooth movement in the cylindrical hole in the phantom, and with the PVC cylinders centered inside and the axes aligned.

The rods are freely interchangeable and can translate parallel to the top phantom surface at a depth of 15 mm (Fig. 1). The coordinate system shown in Fig. 1 is fixed to the phantom block. The center of the top surface is defined as origin (0, 0, 0). The side surface is at $y = 40$ mm. The center of the black cylinder as shown in Fig. 1 is located at (0, 0, 15) mm. During movement, it has the variable position (0, y_{inc}, 15 mm). The source and detector fibers are arranged symmetrically to the axis of the rod and separated by 30 mm. The sizes of the source and detector fibers probes are specified in the next sections, i.e., Secs. 3.1, 3.2 and 3.3, for each system used. When the fibers are attached to the top surface, at positions (−15, 0, 0) mm and (15, 0, 0) mm, the movement of the inclusion corresponds to a lateral scan, with the measuring surface parallel to the inclusion movement. When the fibers are attached to the side surface, at positions (−15, 40, 15) mm and (15, 40, 15) mm, the movement of the inclusion corresponds to a depth scan, with the measuring surface perpendicular to the inclusion movement. The depth of the inclusion, i.e., the distance between center of the inclusion and side surface, is depth = 40 mm − y_{inc}. The rod was then connected to a stepper motor-driven linear actuator that allowed either manual or computer controlled step-wise translational movement of the rod along its axis. Figure 2 shows the photo of the whole experimental setup.

Finally, we note that Table 1 also lists the equivalent $\Delta\mu_a$, i.e., the absorption variation needed for a specific larger inclusion of volume 1 cm^3 to produce the same absorption perturbation, in a diffuse transmittance or reflectance measurement scheme, as the corresponding black cylindrical PVC inclusion. For further details on the definition of the equivalent $\Delta\mu_a$ and the equivalence relation see Ref. 35.

Table 1 Dimensions of the black cylindrical polyvinyl chloride inclusions, and equivalent $\Delta\mu_a$ obtained by using the equivalence relation[35] and assuming an inclusion with a volume of 1 cm^3.

Diameter (mm)	Length (mm)	Volume (mm^3)	Equivalent $\Delta\mu_a$ (cm^{-1})
3	3	21	0.05
4	4	50	0.10
5	5	98	0.17
7	7	269	0.40

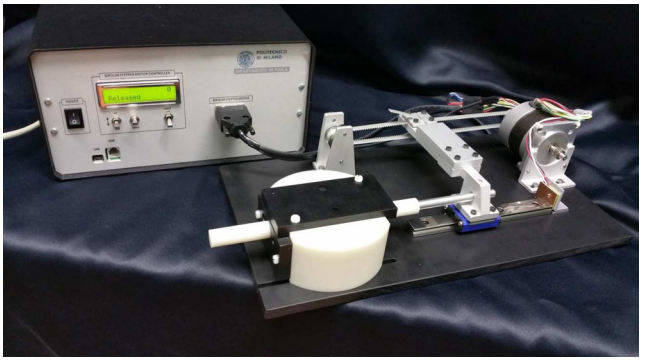

Fig. 2 Photo of the switchable phantom setup. Two black PVC plates were placed on the top and side surfaces to fix the fiber probes in place. The cylindrical rod was connected to a motor-driven linear actuator allowing either manual or computer-controlled translational movement of the rod.

3 Material and Methods

In this section, the experimental setups exploited for characterizing properties and performances of the dynamic phantom, the measurement protocols adopted, and the data analysis procedures implemented are described. In particular, we used three different instruments and approaches for TR near-infrared spectroscopy that are optimized to different aims: (1) to accurately determine the optical properties, i.e., μ_a and μ_s', of the solid homogeneous base material of the phantom; (2) to obtain a two-dimensional transmittance image of the phantom when a black inclusion is inside; and (3) to precisely measure the contrast in optical signal detected in reflectance mode, generated by the black inclusions with different volumes.

3.1 *Time-Resolved Near-Infrared Spectroscopy Setup*

In order to accurately determine the optical properties of the phantom, a state-of-the-art system for TR near-infrared spectroscopy was exploited.[39] The source is a supercontinuum fiber laser (SuperK Extreme, NKT Photonics, Denmark) emitting pulsed white light radiation over the spectral range from 450 to 1750 nm with an overall power of 5 W. Typical pulse duration is in the order of tens of picoseconds, with a repetition rate of 80 MHz. The white light is then dispersed by an F2-glass Pellin-Broca prism (Bernhard Halle Nachfl, Germany) and light of the selected wavelength is focused onto an adjustable slit to achieve better spectral selection. Light is then introduced into a 100 μm graded-index optical fiber and subsequently illuminates the sample. Diffused light is collected using a 1-mm core multimode step-index fiber and separated into two beams by a beamsplitter 50/50 mirror (CM1-BS014, Thorlabs, Germany): half of the collected light is sent to a home-made silicon photomultiplier detector[40] for the detection up to 950 nm, whereas the other half is sent to a photomultiplier tube (H10330A-25, Hamamatsu, Japan) for the detection beyond 950 nm. The electronic signals arising from the detectors are connected to two different time-correlated single-photon counting (TCSPC) boards (SPC-130, Becker & Hickl, Germany) together with the synchronization signal from the laser. The setup is also provided with a reference arm to compensate for the temporal drift of the laser. Further details can be found in Ref. 39.

By means of the TR near-infrared spectroscopy setup described previously, the TR diffuse reflectance of the homogeneous phantom was measured in the wavelength range from 600 to 1200 nm with a resolution of 5 nm and a source–detector separation of 30 mm. Then, the absorption and reduced scattering coefficients of the homogeneous base material were retrieved from the TR curves measured at different wavelengths, by means of a nonlinear least-square fitting procedure exploiting a model for photon migration in diffusive media based on the solution of the diffusion equation with extrapolated boundary conditions in the semi-infinite geometry.[41,42] To improve accuracy, especially at longer wavelengths where the diffusion model is less adequate due to the higher values of absorption and the lower values of scattering, a free time-shift fit was adopted to recover the best fitting parameters (μ_a, μ_s', and time-shift t_0) at 690 nm, where absorption is low.[43] The fitted t_0 was then used as a constant shift all over the spectrum, while fitting μ_a and μ_s' only.

3.2 *Time-Resolved Near-Infrared Imaging Setup*

Images of the phantom with black inclusions inside were obtained by means of an optical mammograph.[44] The instrument is designed to collect projection (transmittance) images of a compressed breast, in the same configuration as conventional x-ray mammography. Seven pulsed diode lasers are used as light sources emitting at 635, 680, and 785 nm (visible, VIS), and at 905, 930, 975, and 1060 nm (near-infrared, NIR), with average output power of a few milliwatts, a pulse width of a few hundreds of picoseconds and a repetition rate of 20 MHz (LDH-P, SEPIA I, PicoQuant GmbH, Germany). Light is injected in the medium by a fiber of diameter 100 μm. The diffusely transmitted light is collected on the side opposite to the source plane, by a fiber bundle of diameter 10 mm whose distal end is bifurcated. Its two legs guide photons to two photomultiplier tubes, one dedicated to the detection for VIS wavelengths (R5900U-01-L16, Hamamatsu, Japan) and the other dedicated for NIR wavelengths (H7422P-60, Hamamatsu, Japan). Two PC boards for TCSPC (SPC-130, Becker and Hickl, Germany) are used for the acquisition of the seven TR transmittance curves.

In order to obtain TR projection images of the phantom, it was positioned between the transparent plates of the TR optical mammograph described previously. The different black inclusions were inserted into the homogeneous block at the center of the phantom. Then, a scanning of the source–detector pair over the phantom was performed in transmittance geometry at 680 nm, by covering an area of 40×40 mm^2 in steps of 2 mm with its center at the position of the inclusion. As reference measurements, images with the inclusions moved outside the scanned area were recorded.

Then, measured TR transmittance curves were processed in order to obtain images for various times: for each pixel of the images, 10 consecutive temporal windows were defined within the whole time period of 5 ns, each having a width of 500 ps. The time origin, $t_w = 0$, was given at the time of the barycenter of the instrument response function. Furthermore, we calculated the time- and space-resolved contrast $C(t_w; x, y)$ produced by the black inclusions with respect to the case of the reference sample

$$C(t_w; x, y) = -\ln \frac{N(t_w; x, y)}{N_0(t_w; x, y)}, \quad (1)$$

where $N(t_w; x, y)$ and $N_0(t_w; x, y)$ are the photon counts integrated over the window starting at the time t_w (delay time),

at position (x, y), obtained when the black inclusion is in the center of the phantom or outside of it, respectively. We note that because $N_0 > N$ and the presence of the logarithm, the contrast C is greater than 0 and can exceed 1. Equation (1) was used to produce the results of Fig. 6.

3.3 *Time-Resolved Functional Near-Infrared Spectroscopy Setup*

Measurements of the perturbations affecting the output signal produced by black inclusions moving inside the homogeneous host phantom were performed exploiting an instrument developed for TR functional near-infrared spectroscopy.[45] This system employs as light sources a couple of picosecond pulsed diode lasers operating at 687 and 826 nm (50 ps full width at half maximum, 80 MHz repetition rate, about 1 mW average power, LDH-P, SEPIA II, PicoQuant GmbH, Germany). An optical switch (2×18 mol, Leoni Fiber Optics GmbH, Germany) allows the implementation of the wavelength space multiplexing approach and the extension of the source channels from 2 up to 16. Laser light illuminates the tissue by means of graded-index multimode glass optical fibers (100/140 μm core/cladding, 0.29 numerical aperture, LighTech srl, Italy). Diffuse light is collected by means of custom-made glass optical fiber bundles (3-mm inner diameter, 0.57 numerical aperture, Loptek Glasfasertechnick GmbH, Germany). Then, the collected light is sent to a hybrid photomultiplier (HPM-100-50, Becker and Hickl GmbH, Germany) by a proper lens system. A custom double band-pass optical filter (OPMI-0037, Semrock, Rochester, NY), centered at 687 and 826 nm is also inserted to decrease the background ambient light. The detection line is completed with a PC board for TCSPC (SPC-130, Becker and Hickl GmbH, Germany). This system has up to eight independent detection lines. A home-made microcontroller unit allows the synchronization between the TCSPC acquisition boards and the optical switch movement during the measurement.

By means of this setup, both lateral and depth scans were performed by a motor-controlled translation of the rod holding the black inclusion inside, for both locations of the source and detector fiber probes as illustrated in Fig. 1. As for the lateral scan, the black inclusion was initially arranged underneath the middle position between the source and detector fibers (at $x = y = 0$) and then moved 29 mm away from this point. This position, with the inclusion far from the fibers, was chosen as the reference or unperturbed state. Starting from this position, the rod was moved in 55 steps of 1 mm. For the depth scan the reference state was chosen by setting one end face of the rod flush with the surface opposite to the fiber probes so that the rod protruded from the host phantom's surface between the fibers with the center of the inclusion (90 mm from both end-faces) located 10 mm outside of the phantom ($y_{\mathrm{inc}} =$ 50 mm). For each step of the rod movement, TR diffuse reflectance was recorded at 687 nm, with a 1 s acquisition time. The laser power was adjusted such that the count rate was about 10^6 s^{-1} in the unperturbed state for each scan.

Before starting the systematic scan measurements, each cylindrical rod was characterized in terms of its angular position; as a matter of fact, any deviation from a concentric location of the black cylinder inside the rod, mainly due to the tolerance of the machining process, may impair the measurement reproducibility. To avoid this uncertainty, we performed a test measurement in the lateral scan geometry, with the black inclusion at $y_{\mathrm{inc}} = 0$, i.e., for maximum contrast. Then, we rotated the rod and identified the angular position where the detected signal attained the mean value between its maximum and minimum. This angular position was kept for the entire set of measurements.

The TR reflectance curves recorded in the lateral and depth scans were processed by defining 10 consecutive time windows of 400-ps width, with a delay time from 0 to 3600 ps), to obtain the time-dependent contrast as a function of the position of the black cylinder inside the phantom y_{inc}, similarly to the case of the imaging measurements

$$C(t_w; y_{\mathrm{inc}}) = -\ln \frac{N(t_w; y_{\mathrm{inc}})}{N_0(t_w)}, \tag{2}$$

where $N(t_w; y_{\mathrm{inc}})$ denotes the photon counts in the time windows t_w at position y_{inc} of the lateral or depth scan, and $N_0(t_w)$ is the photon count in the same time windows with the inclusion at the reference position. Equation (2) was used to produce the results of Figs. 7 and 8.

4 Results: Characterization of the Phantoms, Tests, and Measurements

In this section we report the measurements carried out on the phantom with the three experimental setups described in Sec. 3 that provide a characterization of the phantom at three different levels. In particular, we present the spectral characterization of the bulk optical properties of the phantom (Sec. 4.1), the spatial characterization of the phantom's properties obtained using an imaging system (Sec. 4.2), and finally the homogeneous-to-inhomogeneous switching properties (Sec. 4.3).

4.1 *Bulk Optical Properties*

As part of a basic characterization, we obtained the spectra of the absorption and reduced scattering coefficients of the homogeneous phantom in the wavelength range from 600 to 1200 nm from measurements of diffuse reflectance using the time-domain broadband diffuse spectrometer[39] described in Sec. 3.1. The results are presented in Fig. 3. The absorption spectrum shows an almost constant contribution of the black

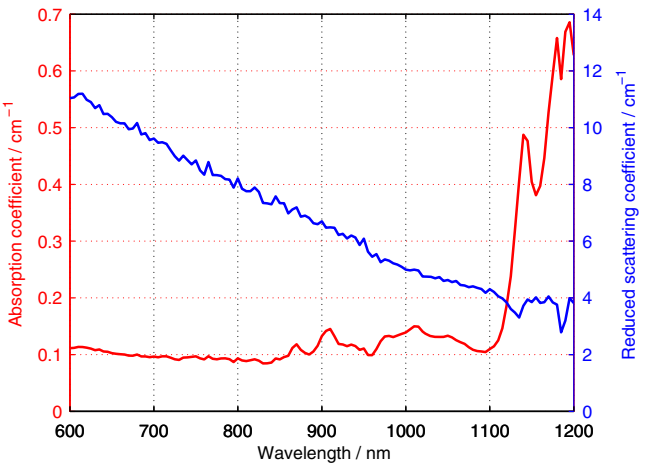

Fig. 3 Absorption and reduced scattering spectra of the bulk phantom material in the 600 to 1200 nm range obtained from time-resolved diffuse reflectance measurements at a source–detector separation of 30 mm.

toner overlapped with the specific spectral features of the epoxy base material in the region beyond 850 nm. The scattering spectrum is rather monotonous and decreasing from 11 cm^{-1} at 600 nm down to 4 cm^{-1} at 1200 nm. The spectral properties presented in Fig. 3 are useful to foresee the applicability of the phantom in a wide wavelength range. In particular, the reduced scattering coefficient at the actual wavelength in use is required to calculate the effective $\Delta\mu_a$ equivalent to the black objects.[35] The related data presented in Table 1 were derived for $\mu_s' = 10$ cm^{-1}, which holds for wavelengths around 700 nm.

4.2 *Transmittance Imaging*

We performed a scan of the phantom in transmittance geometry using the experimental setup described in Sec. 3.2. Figure 4 shows the time-dependent projection images of the phantom for all black inclusions (rows). Images of photon counts in selected time windows $N(t_w; x, y)$ are presented for increasing delay times t_w in steps of 1000 ps (columns). The inclusions are clearly identified in Fig. 4 in the center of the images, with contrast at all delay times, as expected for an absorption perturbation.[46] Although the rod consists of the same material as the bulk phantom, it causes an unwanted intrinsic perturbation in all images. The rod produces a contrast with respect to the surrounding medium that decreases upon increasing time (from 30% at 500 ps down to 10% at 4000 ps). This behavior is nearly the same as one would expect for an increase in scattering or a similar effect.[46]

In order to investigate possible effects due to refractive index mismatches at the interface between the rod and the hosting block, we tried to fill the air gap by immersing the whole phantom in water or lubricating the rod with transparent silicon grease. Figure 5 shows time-integrated (CW) images of the phantom in transmittance geometry using a bare rod with no inclusion inside. The perturbation produced by the rod is clearly visible both for the phantom with no matching fluid [Fig. 5(a)], and in those cases where either water [Fig. 5(ab)], or silicone grease [Fig. 5(c)] was used to fill the air gap around the rod. In the case of water (refractive index $n = 1.33$) the perturbation is milder, but this trend is not confirmed when silicone grease ($n \approx 1.4$) is used to match even closer the refractive index of epoxy ($n \approx 1.5$). Thus, the refractive index mismatch can modulate the visibility of this effect, but seems not to be the real source of the inhomogeneity in the image. The ultimate cause of the perturbation caused by the rod is not yet fully explained and is still under investigation.

Despite the perturbation caused by the cylindrical rod, the concept of the switchable phantom permits to extract the contribution of the inclusion alone by comparing the measurements with and without the inclusion. Figure 6 shows the time-dependent space-resolved contrast $C(t_w; x, y)$, produced by the inclusions and calculated according to Eq. (1). The effect of the rod is almost eliminated, enabling a clear identification of all the four inclusions (rows). The diameter of the peak reflecting the existence of the inclusion increases upon increasing the delay time (columns) as expected due to the spatial broadening of the photon density distribution upon increasing time.

4.3 *Localized Absorption Changes*

The switching properties of the phantom, testing its capability to simulate absorption changes for applications like brain functional imaging, are here characterized by a set of reflectance measurements obtained with the experimental setup described

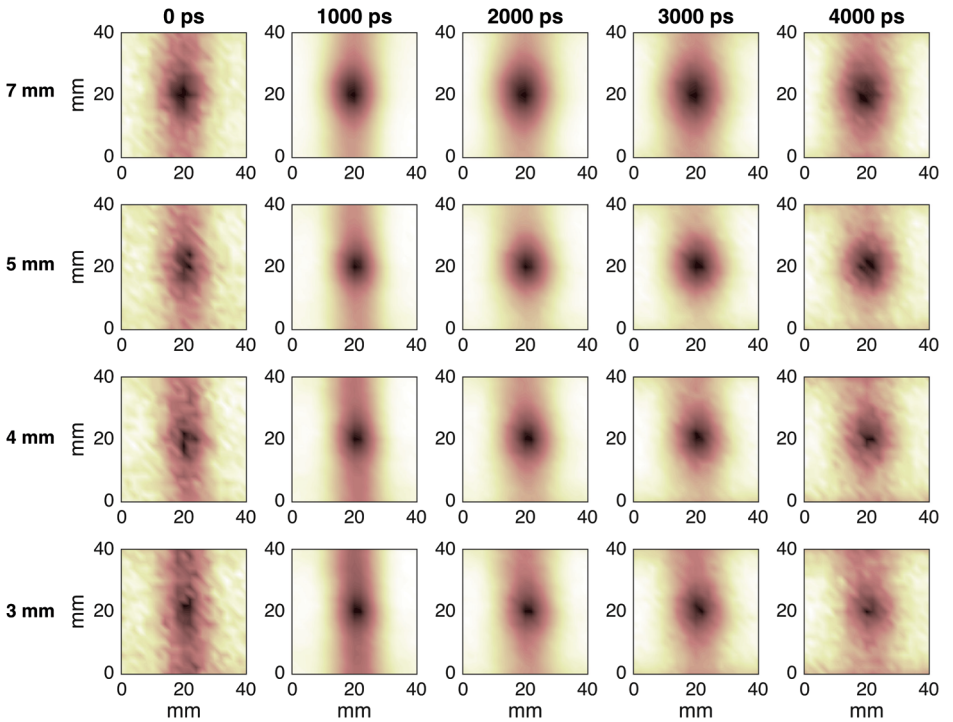

Fig. 4 Transmittance images (photon counts) of the phantom with inclusions of different size (rows) for different time windows (columns). The delay times of the time windows of 500 ps width are indicated at the top. The color scales are adjusted for each panel individually (black: minimum, white: maximum photon count).

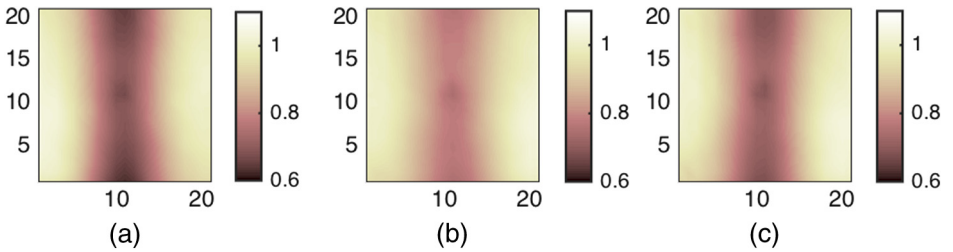

Fig. 5 Time-integrated [continuous-wave (CW)] transmittance images (normalized total photon counts) of the phantom with a homogeneous rod holding no inclusion inside. (a) The same phantom is measured with no matching fluid, and (b) filling the air gap between the rod and the hosting block with water and (c) with silicon grease. All images were normalized to the counts on the unperturbed (white) region and displayed using the same relative scale. The small black dots in the center of the images are caused by a small yet visible scratch caused by the lathe during machining of the phantom block.

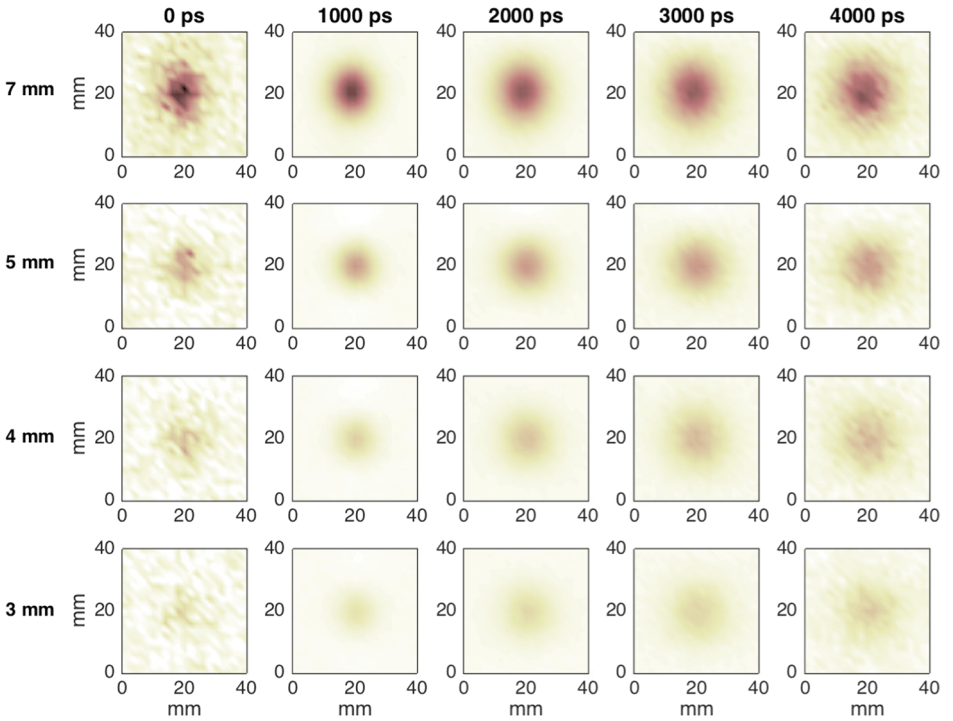

Fig. 6 Time-dependent space-resolved transmittance contrast images, $C(t_w; x, y)$ according to Eq. (1), obtained by relating the images shown in Fig. 4 to images with the rod, but without the black inclusion present. All figures are displayed in the same contrast scale ranging from 0 to 0.7.

in Sec. 3.3. Figure 7 shows the measured contrast $C(t_w; y_{\mathrm{inc}})$ (dashed curves with markers), calculated according to Eq. (2), for a lateral scan, with the inclusion at a depth of 15 mm and a source–detector separation of 30 mm. The results for time windows (width 400 ps) at different delay times t_w (from 0 up to 3600 ps) are displayed for the whole set of inclusions (see Table 1). The four inclusions yield distinct profiles with increasing contrast when increasing the delay time. The theoretical predictions obtained with an 8th-order perturbative model based on the diffusion equation combined with the application of the equivalence relation[35] are also displayed (solid curves). The results of the measurements do not necessarily agree with the theoretical predictions. This can be explained by the fact that the phantom inherently has an inhomogeneous structure in its construction and even when it contains only the pedestal of solid epoxy (unperturbed case) an unwanted and intrinsic contrast perturbation is generated. This is likely the main reason for the disagreement between theoretical predictions and phantom measurements. The trend of the increase in the width and magnitude of the contrast with increase in time for the predictions is quite similar to that for the measurements, but they do not exactly agree with each other. Possible other reasons for discrepancies are the dependence of the contrast on the rotation angle of the rod and the breakdown of the perturbative model for very high-absorption contrasts. The matching of experimental data with an appropriate model is definitely an issue that deserves further investigation; nevertheless, it is not strictly required for the practical use of the phantom. An accurate experimental characterization of the phantom would be sufficient to perform repeatability and reproducibility tests, in particular for quality control of instrument performance during clinical studies, relying on the intrinsic stability of solid phantoms.

Figure 8 shows the contrast $C(t_w; y_{\mathrm{inc}})$ for a depth scan of the inclusion for reflectance measurements, with a source–detector

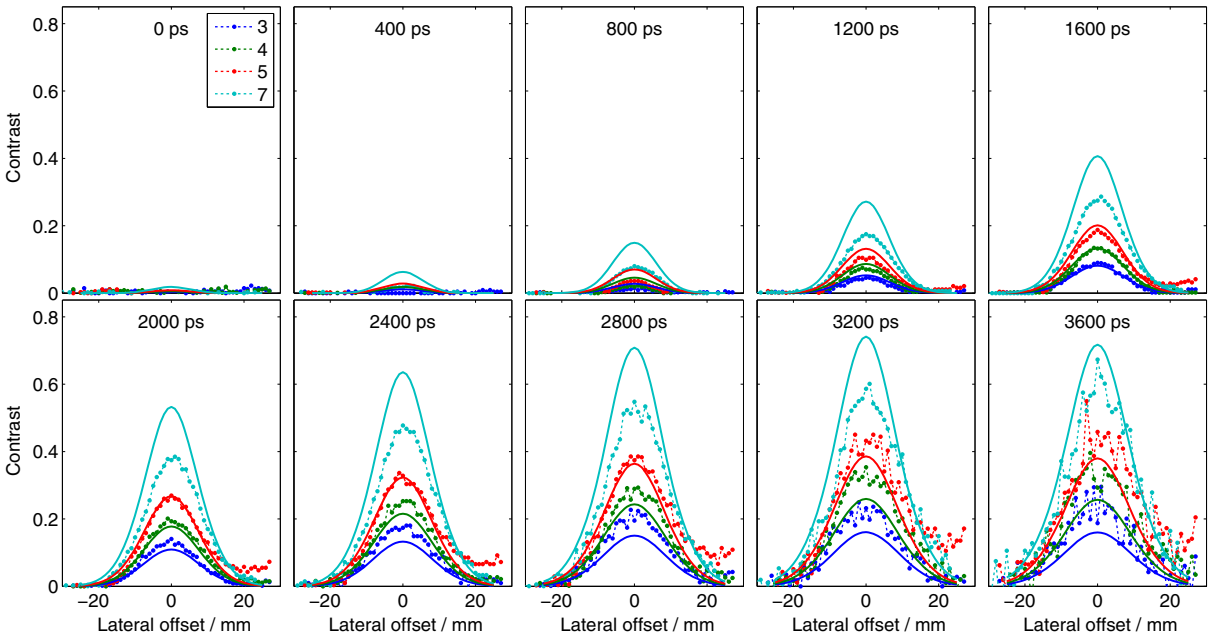

Fig. 7 Contrast $C(t_w; y_{\text{inc}})$ calculated from measured time-resolved (TR) diffuse reflectance for lateral scan. The delay t_w of the time windows is displayed above the panels, while their width is 400 ps. The sizes of the inclusions in mm are given in the legend. The dashed curves with markers represent the measurements while the solid curves are the predictions based on the 8th-order perturbative model.

separation of 30 mm. As for the previous Fig. 7, the results of the experiments (dashed curves with markers) and the theoretical model (solid curves) are shown. When increasing the delay time, the contrast profile is shifted toward a larger depth, with distinct contrast for all four black inclusions. As for the lateral scan, this trend is generally reproduced by the theoretical model, yet with considerable discrepancy. Here, it is worth noting that theoretical descriptions with the inclusion at the external boundary ($y_{\text{inc}} = 40$ mm) are rather critical for the diffusion-based model and for the equivalence relation used in the model. Also, during the depth scan the rod is protruding out of the phantom surface, clearly causing an alteration to the boundary conditions.

So far, the characterization of the phantom by TR transmittance and reflectance measurements was pursued for the purpose of the performance tests of TR diffuse optical instruments.

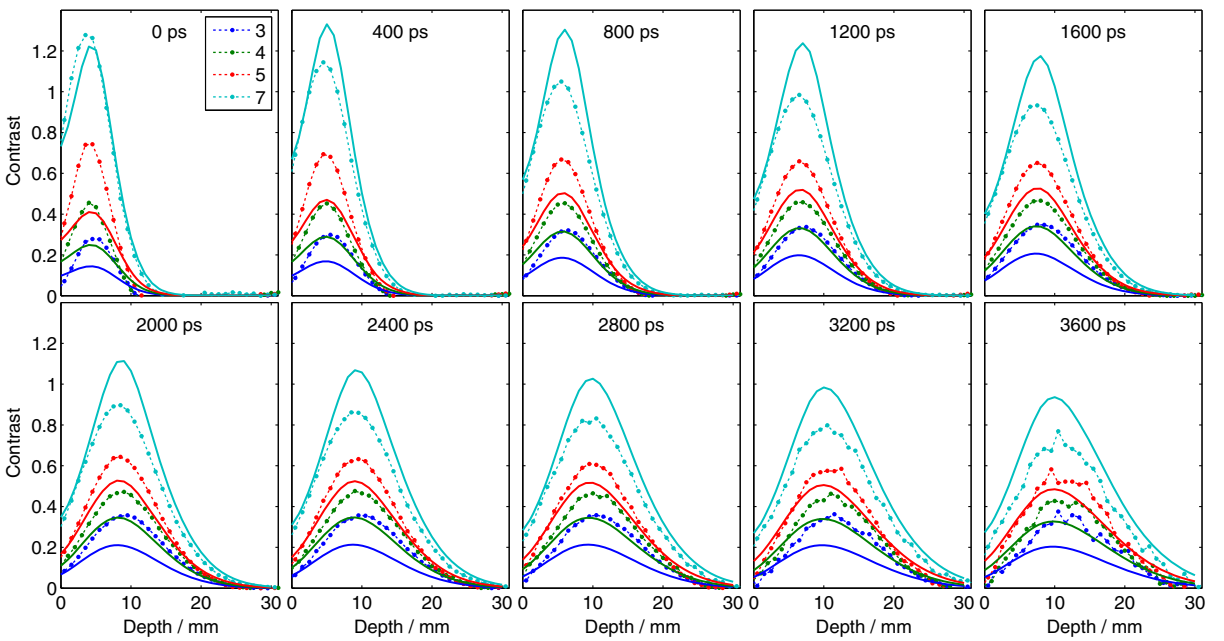

Fig. 8 Contrast C for TR reflectance measurements plotted for a depth scan. The delay of the time windows (left limit) is displayed above the panels, while their width is 400 ps. The size of the inclusions in mm is given in the legend. The dashed curves with markers represent the measurements, and the solid curves the 8th-order perturbative model.

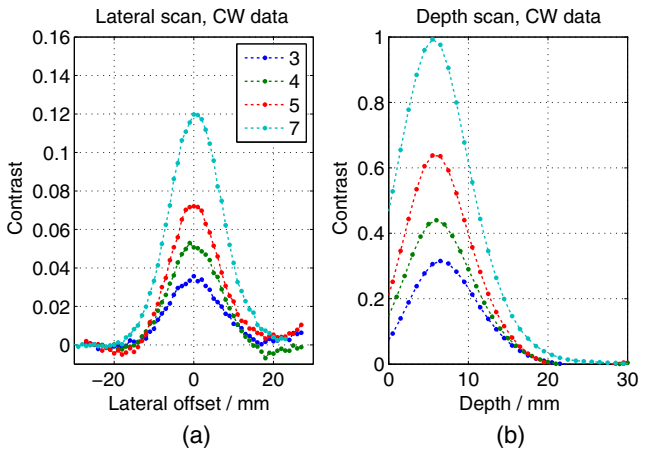

Fig. 9 Contrast C for CW reflectance measurements plotted for: (a) a lateral scan, and (b) a depth scan. The size of the inclusions in mm is given in the legend and can be translated into $\Delta\mu_a$ according to Table 1.

However, the phantom is also suitable for testing CW instruments, as shown in Fig. 9. Both a lateral scan (left panel) and a depth scan (right panel) are presented for the four perturbations. The plots were obtained using the same data as in Figs. 7 and 8, but integrating the TR profiles over the whole time range.

5 Discussion and Future Developments

Different clinical problems can be simulated with the proposed phantom. A major application is functional imaging of the brain where a localized activation, in adults typically about 15 mm beneath the surface, is to be detected based on diffuse reflectance measurements. The type of phantom presented here allows to quantitatively mimic (1) the total attenuation by the tissue, defined by the bulk optical properties of the phantom; (2) the magnitude of the localized change that can be varied by changing the size of the inclusion; and (3) its position in depth. It should be noted that (1) and (2) depend on the source–detector separation and—via the optical properties—on wavelength. This phantom can be employed to implement several important performance tests of the nEUROPt protocol[19] for optical brain imagers.

The results obtained also permit to envisage the use of the proposed phantom for transmittance imaging or even tomography, as in the case of breast imaging. Clearly, the basic assumption is the need to mimic a purely absorbing perturbation as a change with respect to an unperturbed reference state. This is the case, for instance, in neoadjuvant chemotherapy monitoring[9] or in dynamic breast imaging.[32]

The present implementation and characterization of the proposed phantom concept can be further improved. The origin of the signal disturbances due to the discontinuity of the rod is still unclear and requires further investigations, in order to reduce or possibly eliminate it. In addition, by a more precise machining it might be possible to minimize the effects related to the rotation of the rod about its axis. A better characterization in terms of accuracy, stability, and durability of the phantom's optical properties will be a next step towards its further development as a standardized tool for the evaluation of the performances of diffuse optics instruments. Moreover, the theoretical modeling of the phantom is still inadequate. Further studies could improve on these aspects and propose more advanced solutions. Surely, the high accuracy attainable with liquid–solid inhomogeneous phantoms[23] has to be evaluated and compared to the tremendous easiness, ruggedness, and potential of commercialization of the new all-solid approach.

6 Conclusions

We have presented a new concept for the design of mechanically switchable solid inhomogeneous phantoms simulating a localized absorption change. The adoption of an epoxy-based solid phantom approach implies all advantages in terms of stability, durability, ease of use, and aptness for clinical or industrial quality control that are inherent to the solid phantom solution. The use of black inclusions—which greatly simplifies the phantom fabrication—is based on the equivalence relation between any given realistic absorption perturbation and a totally absorbing inclusion with an appropriate volume. Two modes of changing the position of the inclusion with respect source and detector were demonstrated: (1) lateral scan with the measuring surface parallel to the inclusion movement; and (2) depth scan with the measuring surface perpendicular to the inclusion movement. Another novel feature is the opportunity to realize a dynamic absorption change by translating a rod holding a small black inclusion with an adjustable speed.

A practical realization of such a phantom was described and characterized by various time-domain diffuse optics instruments in terms of absorption and scattering spectra in the 600 to 1200 nm range, transmittance images, and lateral and depth scans in reflectance geometry. However, the application of the proposed phantom is not limited to time-domain systems, and CW and frequency-domain instruments can be characterized by means of this type of phantom as well.

There are still some aspects to be improved such as the unwanted perturbation produced by the movable rod embedding the inclusion or the suboptimal match with the theoretical model. Nevertheless, even in its present form, the constructed phantom can be used for easy and quick performance tests, provided that an experimental characterization of the phantom is performed in advance and provided as a data-sheet.

Acknowledgments

The research leading to these results has partially received funding from the European Commission under the projects LASERLAB-EUROPE (Grant Agreement No. 284464), OILTEBIA (Grant Agreement No. 317526, FP7-PEOPLE-2012-ITN), and BabyLux (Grant Agreement No. 620996, CIP-ICT-PSP-2013-7).

References

1. T. Durduran et al., "Diffuse optics for tissue monitoring and tomography," *Rep. Prog. Phys.* **73**(7), 076701 (2010).
2. M. Ferrari and V. Quaresima, "A brief review on the history of human functional near-infrared spectroscopy (fNIRS) development and fields of application," *NeuroImage* **63**(2), 921–935 (2012).
3. D. A. Boas et al., "Twenty years of functional near-infrared spectroscopy: introduction for the special issue," *NeuroImage* **85**(1), 1–5 (2014).
4. P. A. Delgado, G. Schwarz, and G. E. Klein, "NIRS matrix: a new tool in neuromonitoring during interventional neuroradiology: A-391," *Eur. J. Anaesthesiol.* **23**, 104 (2006).
5. B. Bhatia et al., "The application of near-infrared oximetry to cerebral monitoring during aneurysm embolization: a comparison with intraprocedural angiography," *J. Neurosurg. Anesthesiol.* **19**(2), 97–104 (2007).

6. H. Maslehaty et al., "Continuous measurement of cerebral oxygenation with near-infrared spectroscopy after spontaneous subarachnoid hemorrhage," *ISRN Neurol.* **2012**, 907187 (2012).
7. D. R. Leff et al., "Diffuse optical imaging of the healthy and diseased breast: a systematic review," *Breast Cancer Res. Treat.* **108**(1), 9–29 (2008).
8. A. Poellinger et al., "Breast cancer: early- and late-fluorescence near-infrared imaging with indocyanine green–a preliminary study," *Radiology* **258**(2), 409–416 (2011).
9. R. Choe et al., "Diffuse optical tomography of breast cancer during neoadjuvant chemotherapy: a case study with comparison to MRI," *Med Phys.* **32**(4), 1128–1139 (2005).
10. L. Enfield et al., "Monitoring the response to neoadjuvant hormone therapy for locally advanced breast cancer using three-dimensional time-resolved optical mammography," *J. Biomed. Opt.* **18**(5), 056012 (2013).
11. A. Torricelli et al., "Time-resolved reflectance spectroscopy for non-destructive assessment of food quality," *Sens. Instrum. Food Qual. Saf.* **2**, 82–89 (2008).
12. M. Zude (Ed.), *Light Optical Monitoring of Fresh and Processed Agricultural Crops, (Contemporary Food Engineering Series)*, CRC Press, Boca Raton, Florida (2009).
13. A. Kienle et al., "Light propagation in dry and wet softwood," *Opt. Express* **16**(13), 9895–9906 (2008).
14. C. D'Andrea et al., "Time-resolved optical spectroscopy of wood," *Appl. Spectrosc.* **62**(5), 569–574 (2008).
15. J. Johansson et al., "Time-resolved NIR/Vis spectroscopy for analysis of solids: pharmaceutical tablets," *Appl. Spectrosc.* **56**(6), 725–731 (2002).
16. D. Khoptyar et al., "Broadband photon time-of-flight spectroscopy of pharmaceuticals and highly scattering plastics in the VIS and close NIR spectral ranges," *Opt. Express* **21**(17), 20941–20953 (2013).
17. J. Hwang, J. C. Ramella-Roman, and R. Nordstrom, "Introduction: feature issue on phantoms for the performance evaluation and validation of optical medical imaging devices," *Biomed. Opt. Express* **3**(6), 1399–1403 (2012).
18. H. Wabnitz et al., "Performance assessment of time-domain optical brain imagers, part 1: basic instrumental performance protocol," *J. Biomed. Opt.* **19**(8), 086010 (2014).
19. H. Wabnitz et al., "Performance assessment of time-domain optical brain imagers, part 2: nEUROPt protocol," *J. Biomed. Opt.* **19**(8), 086012 (2014).
20. A. Pifferi et al., "Performance assessment of photon migration instruments: the medphot protocol," *Appl. Opt.* **44**(11), 2104–2114 (2005).
21. A. E. Cerussi et al., "Tissue phantoms in multicenter clinical trials for diffuse optical technologies," *Biomed. Opt. Express* **3**(5), 966–971 (2012).
22. A. M. De Grand et al., "Tissue-like phantoms for near-infrared fluorescence imaging system assessment and the training of surgeons," *J. Biomed. Opt.* **11**(1), 014007 (2006).
23. F. Martelli et al., "Phantoms for diffuse optical imaging based on totally absorbing objects, part 2: experimental implementation," *J. Biomed. Opt.* **19**(7), 076011 (2014).
24. L. Spinelli et al., "Determination of reference values for optical properties of liquid phantoms based on Intralipid and India ink," *Biomed. Opt. Express* **5**(7), 2037–2053 (2014).
25. G. Lamouche et al., "Review of tissue simulating phantoms with controllable optical, mechanical and structural properties for use in optical coherence tomography," *Biomed. Opt. Express* **3**(6), 1381–1398 (2012).
26. B. W. Pogue and M. S. Patterson, "Review of tissue simulating phantoms for optical spectroscopy, imaging and dosimetry," *J. Biomed. Opt.* **11**(4), 041102 (2006).
27. H. Jiang et al., "Frequency-domain optical image reconstruction in turbid media: an experimental study of single-target detectability," *Appl. Opt.* **36**(1), 52–63 (1997).
28. J. P. Culver et al., "Three-dimensional diffuse optical tomography in the parallel plane transmission geometry: evaluation of a hybrid frequency domain/continuous wave clinical system for breast imaging," *Med. Phys.* **30**(2), 235–247 (2003).
29. R. Cubeddu et al., "Time-resolved imaging on a realistic tissue phantom: μ_s' and μ_a images versus time-integrated image," *Appl. Opt.* **35**(22), 4533–4540 (1996).
30. S. Carraresi et al., "Accuracy of a perturbation model to predict the effect of scattering and absorbing inhomogeneities on photon migration," *Appl. Opt.* **40**(25), 4622–4632 (2001).
31. R. Cubeddu et al., "A solid tissue phantom for photon migration studies," *Phys. Med. Biol.* **42**(10), 1971–1979 (1997).
32. J. C. Hebden et al., "An electrically-activated dynamic tissue-equivalent phantom for assessment of diffuse optical imaging systems," *Phys. Med. Biol.* **53**(2), 329–337 (2008).
33. A. Gibson et al., "Optical tomography of a realistic neonatal head phantom," *Appl. Opt.* **42**(16), 3109–3116 (2003).
34. T. Funanen et al., "Dynamic phantom with two stage-driven absorbers for mimicking hemoglobin changes in superficial and deep tissues," *J. Biomed. Opt.* **17**(4), 047001 (2012).
35. F. Martelli et al., "Phantoms for diffuse optical imaging based on totally absorbing objects, part 1: basic concepts," *J. Biomed. Opt.* **18**(1), 066014 (2013).
36. R. Barbour et al., "Validation of near infrared spectroscopic (NIRS) imaging using programmable phantoms," *Proc. SPIE* **6870**, 687002 (2008).
37. R. Barbour et al., "A programmable laboratory testbed in support of evaluation of functional brain activation and connectivity," *IEEE Trans. Neural Syst. Rehabil. Eng.* **20**(2), 170–183 (2012).
38. J. Swartling, J. S. Dam, and S. Andersson-Engels, "Comparison of spatially and temporally resolved diffuse-reflectance measurement systems for determination of biomedical optical properties," *Appl. Opt.* **42**(22), 4612–4620 (2003).
39. I. Bargigia et al., "Diffuse optical techniques applied to wood characterisation," *J. Near Infrared Spectrosc.* **21**(4), 259–268 (2013).
40. A. D. Mora et al., "Towards next-generation time-domain diffuse optics for extreme depth penetration and sensitivity," *Biomed. Opt. Express* **6**(5), 1749–1760 (2015).
41. D. Contini, F. Martelli, and G. Zaccanti, "Photon migration through a turbid slab described by a model based on diffusion approximation. I. Theory," *Appl. Opt.* **36**(19), 4587–4599 (1997).
42. F. Martelli et al., *Light Propagation through Biological Tissue and Other Diffusive Media: Theory, Solutions and Software*, SPIE Press, Bellingham, Washington (2010).
43. R. Cubeddu et al., "Experimental test of theoretical models for time-resolved reflectance," *Med. Phys.* **23**(9), 1625–1634 (1996).
44. P. Taroni et al., "Seven-wavelength time-resolved optical mammography extending beyond 1000 nm for breast collagen quantification," *Opt. Express* **17**(18), 15932–15946 (2009).
45. R. Re et al., "Multi-channel medical device for time domain functional near infrared spectroscopy based on wavelength space multiplexing," *Biomed. Opt. Express* **4**(10), 2231–2246 (2013).
46. R. Cubeddu et al., "Imaging of optical inhomogeneities in highly diffusive media: discrimination between scattering and absorption contributions," *Appl. Phys. Lett.* **69**(27), 4162–4164 (1996).

Biographies of the authors are not available.